



Unveiling the synergistic effect between the metallic phase and bridging S species over MoS₂ for highly efficient nitrogen fixation

Ruoqi Liu^a, Hao Fei^a, Jian Wang^b, Ting Guo^a, Fangyang Liu^c, Zhuangzhi Wu^{a,*}, Dezhi Wang^{a,*}

^a School of Materials Science and Engineering, Central South University, Changsha 410083, China

^b School of Energy and Environment, City University of Hong Kong, Kowloon, the Hong Kong Special Administrative Region of China

^c School of Metallurgy and Environment, Central South University, Changsha 410083, China

ARTICLE INFO

Keywords:

Nitrogen reduction reaction
Molybdenum sulfide
Phase engineering
Hydrogen evolution reaction
Bridging sulfur

ABSTRACT

Electrocatalytic nitrogen reduction reaction (NRR) is considered an appealing approach towards sustainable NH₃ production but still undergoes serious challenges with unsatisfactory catalytic performance, which hinders its large-scale application. In this work, the S-rich 1T-MoS₂ with an ultrahigh 1T phase content and S-enrichment has been successfully synthesized and firstly verified as an exceptional NRR catalyst with high activity and selectivity. The optimized MoS_{2.30} catalyst exhibits a high NH₃ yield rate (98.30±1.63 μg h⁻¹ mg_{cat}⁻¹) and FE (23.10±0.38%), surpassing nearly all the reported MoS₂-based NRR catalysts and the overwhelming majority of advanced NRR catalysts, demonstrating the encouraging role-playing of the synergistic effect between 1T phase and bridging S₂²⁻ species on NRR performances. DFT calculations reveal that the high properties empowered by MoS_{2.30} are on account of the synergistic effect that induces the enhanced NRR activity via the strengthened N₂ adsorption and reduced energy barrier (E_b) as well as the improved NRR selectivity through the optimized competitive adsorption and reduced energy barrier against the hydrogen evolution reaction (HER). This work fabricates a MoS₂-based electrocatalyst for highly efficient NRR and proves an effective strategy to improve the catalytic performance, which is worth being extended to other catalytic reactions.

1. Introduction

Electrochemical NRR, emerging to be a vital component in the next-generation electrochemical energy conversion field, has drawn great attention to substitute the Haber-Bosch process [1,2]. Unfortunately, the roadblock lying in access to highly effective ammonia production emanates from the unsatisfied ability of electrocatalysts to wreck the stable N≡N bond and defeat the strongly competitive HER, causing poor NRR activity and selectivity, respectively [3–5]. To resolve this bottleneck, it is highly required to develop the design concept of NRR electrocatalysts with excellent catalytic activity and selectivity.

Mimicked from the molybdenum-iron-sulfur active centers of nitrogenase, molybdenum sulfide (MoS₂), as a typical layered transition metal dichalcogenide, has currently been deemed as a desirable catalyst for NRR [6–8]. Nonetheless, its NRR performance is still far less satisfactory owing possibly to the limited available edges as active sites and poor conductivity [6,9]. In contrast, the metallic 1T-MoS₂ owns more active sites (edges and basal plane) and splendid electronic conductivity, rendering fascinating benefits for electrocatalysis towards NRR [10],

including 1T-MoS₂/g-C₃N₄ [11], CNMS [12], Fe_{0.1}Mo_{0.9}S₂ [13], etc. Nonetheless, the impact of S-sites on NRR performance over the 1T phase has not been fully characterized by experimental research. On the one hand, the presence of bridging S₂²⁻ species can trigger the surrounding electron redistribution and benefit the conductivity. On the other hand, the intercalation of bridging S₂²⁻ species may stabilize the 1T phase to some extent [14]. The above information serves for specifically designing S-rich 1T-MoS_x materials that eventually lead to an efficient NRR electrocatalyst.

In this work, we employed a hydrothermal method to derive non-stoichiometric high phase-purity 1T-MoS₂ nanosheets (MoS_x) with S enrichment, where the phase transition was induced in the weak acid environment. The optimized S-rich 1T-MoS₂ with a stoichiometry of MoS_{2.30} succeeds over the majority of NRR catalysts with outstanding NH₃ yield rate (98.30±1.63 μg h⁻¹ mg_{cat}⁻¹) and FE (23.10±0.38%) at −0.5 V versus reversible hydrogen electrode (vs. RHE), demonstrating the tremendous roles of the synergistic effect between the 1T phase and bridging S species on NRR performance. Besides, we performed density functional theory (DFT) calculation aiming at predicting multiple

* Corresponding authors.

E-mail addresses: zwu@csu.edu.cn (Z. Wu), dzwang@csu.edu.cn (D. Wang).

<https://doi.org/10.1016/j.apcatb.2023.123469>

Received 20 September 2023; Received in revised form 26 October 2023; Accepted 3 November 2023

Available online 5 November 2023

0926-3373/© 2023 Elsevier B.V. All rights reserved.

models of S-rich 1T-MoS₂ under the assumption that the extra S species could bond with the S atoms to form the bridging ligand and/or substitute the Mo atoms. Considering the calculated Gibbs free energy for N₂ adsorption and E_b of the potential-determining step (PDS) in the NRR process, the best model is the S adatoms comprising additional S atoms bridging the two MoS₂ slabs (S^B), in-plane S atom (S^I), and one S atom substituted for one Mo atom in each layer (S^{Mo}) together, proving the joint contributions of the bridging S and 1T phase and firmly validating the experimental results.

2. Experimental section

2.1. Catalyst preparation

The 1T/2H-MoS₂ catalysts were prepared through a facile one-step hydrothermal reaction based on previous work [15]. In a typical synthesis procedure, 1 mmol of Na₂MoO₄·2H₂O and 5 mmol of CS(NH₂)₂ were dissolved in a mixed solvent containing 16 mL of deionized water and 8 mL of acetic acid. The mixture was magnetically stirred for 10 min, then poured into a 50 mL Teflon-lined autoclave, and heated in an electric oven at 180 °C for 4 h. The autoclave was then allowed to cool to room temperature naturally, and the product with the molybdenum-sulfur mole ratio of 1:2.30 was collected after centrifugation. Finally, black powder was rinsed with deionized water and ethanol several times and then dried at 60 °C under vacuum, named as MoS_{2.30}. In a control experiment, the pristine MoS₂ without adding acetic acid was synthesized from identical precursors through the hydrothermal treatment at 220 °C for 24 h, named as MoS₂/P. Moreover, the obtained MoS_{2.30} was annealed in a tube furnace at 800 °C for 2 h under an argon atmosphere to get the A-MoS_{2.30} sample. To remove the excess S species of MoS_{2.30} for further comparison, 100 mg MoS_{2.30} powder was dissolved in 15 mL ultrapure water containing 60 mg NaBH₄, followed by ultrasonic treatment for 2 h, the final sample was denoted as r-MoS_{2.30}.

Besides, the S-rich 1T-MoS₂ with various S/Mo stoichiometry (2.11, 2.19, 2.38, and 2.45) could be facilely available by a one-step hydrothermal process in the acidic conditions with a series of thiourea amounts (3, 4, 6, and 7 mmol), and the obtained samples were labeled as MoS_{2.11}, MoS_{2.19}, MoS_{2.38}, and MoS_{2.45}, respectively.

2.2. Characterization

The X-ray diffraction (XRD) patterns were collected on a D/max-2500 X-ray Diffractometer with a Cu Kα radiation (λ=1.54 Å). The Raman spectra were obtained using the LabRAMHR-800 (HORIBA, French) at 633 nm. The X-ray photoelectron spectroscopy (XPS) measurements were performed on an ESCALAB 250 Xi using Al Kα as the exciting source. The scanning electron microscopy (SEM) images were captured using a FEI Sirion 200 scanning electron microscope. The transmission electron microscopy (TEM) and high-resolution TEM (HRTEM) images were collected on a JEOL-2100 F transmission electron microscope. The binding energy value of each element was calibrated with C 1 s at 284.6 eV. The X-ray absorption spectroscopy (XAS) at the Mo K-edge was collected at Beamline TLS, National Synchrotron Radiation Research Center, Taiwan, Experimental Facility Division X-ray Absorption Group. X-ray absorption near edge structure (XANES) and extended X-ray absorption fine structure (EXAFS) data were analyzed using the ATHENA program.

2.3. Calculations of NH₃ formation rate and FE

The FE for the N₂ reduction was defined as the amount of electric charge which was used for synthesizing NH₃ divided the total charge passed through the electrodes during the electrolysis. The total amount of NH₃ was measured using colorimetric methods. Assuming three electrons were needed to produce one NH₃ molecule, the FE could be

calculated as follows:

$$FE = \frac{3 \times F \times [NH_4^+] \times V}{17 \times Q} \quad (1)$$

The rate of NH₃ formation was calculated using the following equation:

$$\text{Ammonia formation rate} = \frac{[NH_4^+] \times V}{m \times t} \quad (2)$$

Where *F* is the Faraday constant (96485.3 C mol⁻¹), [NH₄⁺] is the measured NH₃ concentration, *V* is the volume of the cathodic reaction electrolyte, *Q* is the quantity of applied electricity, *t* is the reduction time and *m* is the catalyst mass.

For more details, please see the Appendix A [Supplementary data](#).

3. Results and discussion

3.1. Characterization of the samples

A profile representation describing the synthesis of MoS_x is shown in Fig. 1a. The S-rich 1T-MoS₂ with various S/Mo stoichiometry (2.11, 2.19, 2.30, 2.38, and 2.45) could be facilely available by a one-step hydrothermal process in the acidic conditions with a series of thiourea amounts (3, 4, 5, 6, and 7 mmol), and the obtained samples were labeled as MoS_{2.11}, MoS_{2.19}, MoS_{2.30}, MoS_{2.38}, and MoS_{2.45}, respectively. Besides, pristine MoS₂ (MoS₂/P) was synthesized following the same procedure without adding acetic acid. For comparison, the MoS_{2.30} was further treated by a chemical etching method using NaBH₄ as the reductant to remove the excess S species (marked as r-MoS_{2.30}), and it was annealed to retransfer to 2H phase (denoted as A-MoS_{2.30}). The scanning electron microscopy (SEM) image (Fig. 1b) of MoS_{2.30} assembled into nanoflower-like spheres is composed of layered nanosheets with lateral sizes ranging from 200 to 400 nm, additionally evidenced by the transmission electron microscopy (TEM) image (Fig. 1c), whereas the MoS₂/P in Fig. S1 displays a much larger diameter of 1–2 μm. Smaller particles of MoS_{2.30} can be attributed to the confined crystal growth caused by the acidic conditions and excess thiourea, thus significantly increasing the number of active sites [15,16]. Typical crystal lattices of the MoS_{2.30} (6.3 Å) are presented in the high-resolution TEM (HRTEM) image (Fig. 1d) [15].

In reality, two alternative structural arrangements in MoS₂ (Fig. 1e), including the triangular coordination octahedral structure representing the 1T phase and the honeycomb-like trigonal shape denoting the 2H phase, are clearly displayed in Fig. 1f and g, respectively [12,17,18]. However, the extra S atoms cannot be detected because of the TEM instrument limitation, but many disordered regions can be easily distinguished (the yellow dash circle in Fig. 1e), indicating the amorphous nature of the samples induced by the extra S atoms, which is remarkably different from the 1T-MoS₂ with well crystalline in our previous report [12]. In addition, energy-dispersive X-ray (EDX) mapping images demonstrate Mo and S elements are homogeneously distributed in MoS_{2.30}, as revealed in Fig. S2.

Fig. 2a depicts the X-ray diffraction (XRD) characterization of the samples, where both the A-MoS_{2.30} and MoS₂/P exhibit the typical MoS₂ peaks (JCPDS 37–1492). However, all the peaks of MoS_{2.30} noticeably become broadened, confirming its amorphous nature [19,20], consistent with HRTEM results (Fig. 1e). Note that the characteristic peaks of the 1T phase cannot be facilely distinguished due to the similar peak positions of the 1T and 2H phases and the wide peaks of MoS_{2.30}, indicating that the crystal lattice of MoS₂ has no remarkable changes during the generation of the metallic phase induced by the acidic conditions [21,22]. While, as depicted in Fig. 2b, the 1T phase could be definitely confirmed by the Raman signals of MoS₂/P and MoS_{2.30} at 148, 212, 282, and 335 cm⁻¹, which are in accordance with the J₁, J₂, E_{1g}, and J₃ vibrations of metallic phase, respectively [23–25]. Comparatively, the A-MoS_{2.30} just displays two sharp signals around 378 and 408 cm⁻¹,

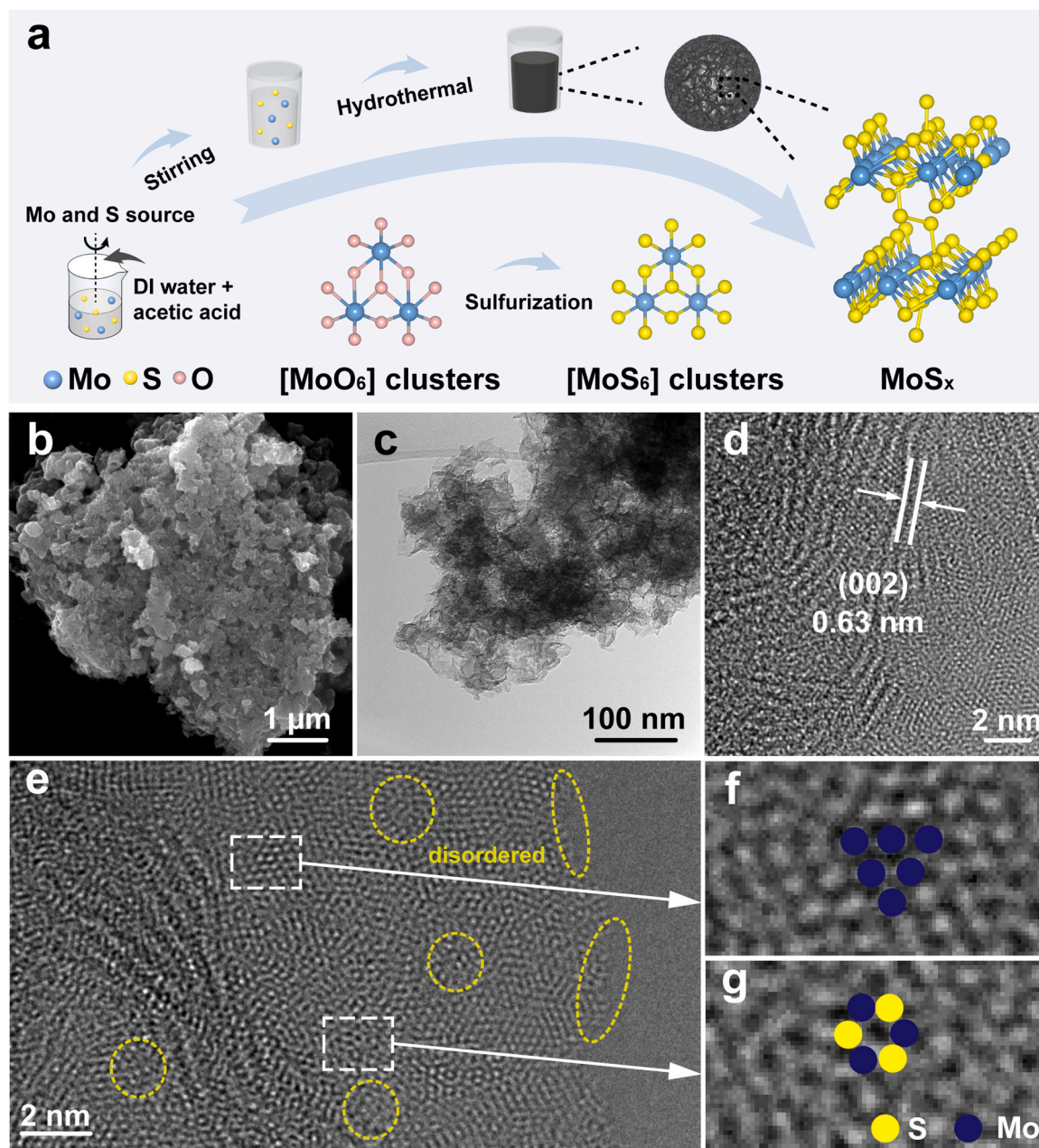


Fig. 1. (a) Synthesis schematic illustration of MoS_x. (b) SEM, (c) TEM, and (d, e) HRTEM images of MoS_{2.30}. (f, g) images of the region enclosed by the white rectangle of (e).

belonging to the E_{2g}^1 and A_{1g} modes of 2H-MoS₂, respectively, suggesting the phase re-transition during annealing [26,27]. The X-ray photoelectron spectroscopy (XPS) spectra in the Mo 3d region of MoS₂/P and MoS_{2.30} possess two doublets (Fig. 2c), and the one at 232.4 and 229.2 eV is derived from the 2H phase [24,28], while the other dual at 231.5 and 228.3 eV with a red-shift of 1.0 eV identify the existence of 1T-MoS₂ [29,30]. Fig. 2d displays the S 2p spectra of MoS₂/P related to the terminal S²⁻ species of 1T and 2H phase, respectively [31–33]. As for MoS_{2.30}, two additional peaks can be clearly observed, which are associated with the bridging S₂²⁻ species originating from excess S species [14,34,35]. Furthermore, the typical 2H-MoS₂ characteristic peaks of A-MoS_{2.30} in Fig. 2c and d also verify the increased crystallinity and 1T-to-2H transformation, corresponding to the XRD and Raman data (Fig. 2a and b). According to Mo 3d deconvolution results, the 1T phase content is approximately 93.31% in MoS_{2.30}, more than twice as high as that in MoS₂/P (42.37%), strongly revealing the effectively induced role

of the acidic environment on the formation of 1T phase. After chemical etching of MoS_{2.30}, the content of bridging S₂²⁻ species over r-MoS_{2.30} sharply decreases (Fig. S3), while the terminal S²⁻ species and the 1T content have a tiny change (91.14%), indicating that bridging S₂²⁻ species are mainly etched owing to more unstable nature compared with terminal S²⁻ species and have a negligible effect on the 1T phase [36]. In comparison with that of the A-MoS_{2.30} (Fig. 2e), the X-ray absorption near-edge spectroscopy (XANES) spectra of MoS_{2.30} and r-MoS_{2.30} negatively shift, demonstrating a reduced Mo valence state induced by the electronic import in the 1T phase during the material synthesis, which matches well with the XPS results (Fig. 2c and S3) [37,38]. Further analysis reveals that there is a slight positive shift for r-MoS_{2.30} compared to MoS_{2.30}, which may be caused by the loss of bridging S₂²⁻ species etched by NaBH₄. The Fourier transform extended X-ray absorption fine structure (FT EXAFS) spectra of A-MoS_{2.30} (Fig. 2f and S4) shows the signals at 2.41 and 3.17 Å, matching with the Mo-S and

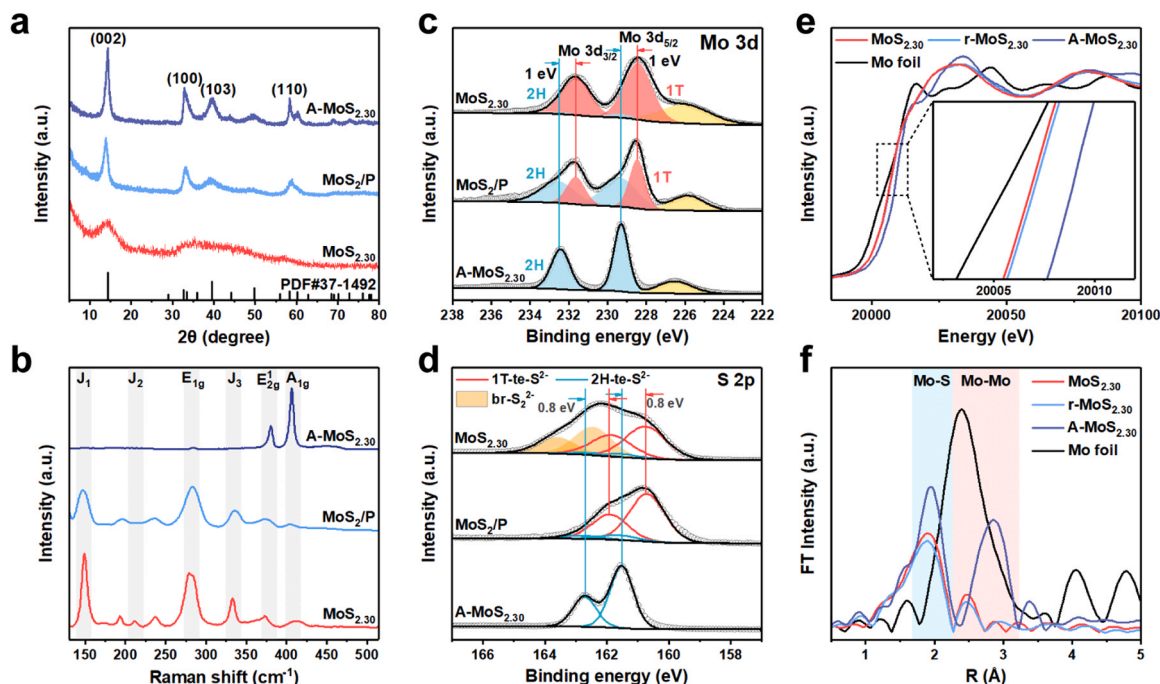


Fig. 2. (a) XRD patterns, (b) Raman spectra, and XPS spectra in (c) Mo 3d and (d) S 2p regions over MoS₂/P, MoS_{2.30}, and A-MoS_{2.30}. (e) Normalized XANES spectra and (f) the corresponding Fourier transform of Mo K-edge EXAFS spectra.

Mo-Mo shell of the 2H phase, respectively [37]. In comparison, MoS_{2.30} and r-MoS_{2.30} exhibit a shortened Mo-Mo bond (2.75 Å) and a reduced bond intensity for the two signals, indicating the reduced coordination number of Mo-S and Mo-Mo bonds in MoS_{2.30} and r-MoS_{2.30}, which should be ascribed to the distorted 1T phase, in accordance with the XRD and TEM results [39,40]. Moreover, after removing the excess bridging S₂²⁻ species, r-MoS_{2.30} shows a further declined peak intensity than those of MoS_{2.30}, indicating the reduced coordination number.

As displayed in Figs. S5 and S6, we find that the creation of the 1T-MoS₂ induced by the weak acid conditions firstly undergoes the reduction of the Mo (VI) species to form the [MoO₆] cluster, followed by the sulphuration to generate 1T phase. According to the findings above, the content of the 1T phase was optimized to 93.31% using 8 mL acetic acid (MoS_{2.30}, Fig. S7). Besides, by further modulating the molar ratio of reactants, the samples with different stoichiometric ratios (2.11, 2.19, 2.38, and 2.45) were prepared, denoted as MoS_{2.11}, MoS_{2.19}, MoS_{2.38}, and MoS_{2.45}, respectively (Fig. S8 and Table S1). With the increased amount of thiourea, the 1T phase proportion is maintained, while the bridging S₂²⁻ increases, indicating that the excess thiourea mainly introduces the bridging S₂²⁻ species with no effect on the generation of 1T phase. Moreover, the stoichiometric ratio of r-MoS_{2.30} is 2.01, suggesting the effective etching (Fig. S3 and Table S1). Overall, the S-rich 1T-MoS₂ with different contents of 1T phase and bridging S₂²⁻ species can be easily regulated by changing the amount of acetic acid and thiourea, respectively.

3.2. NRR performance of the samples

The electrocatalyst suspension, coated on the glassy carbon electrode at room temperature, served as the working electrode. Prior to the electrocatalysis, the feeding N₂ was sufficiently purified using the in-line acid and alkaline trap aiming at removing the potential N impurities [41–43]. After purification, the presence of NO₃⁻ and NO₂⁻ was quantitatively traced to eliminate the possible contamination derived from the nitrogen oxides (NO_x) in the electrolyte or the feeding gas (Fig. S9). One can see that there are no obvious signals at the corresponding locations in the spectra before and after purification, demonstrating that there are

almost no nitrogen oxide pollutants in the electrolyte or the feeding gas. Figs. S10 and S11 show the calibration curves detecting the produced NH₃ and the potential byproduct of N₂H₄ [12]. The NRR performance of MoS_{2.30}, MoS₂/P, and A-MoS_{2.30} are displayed in Fig. S12. In contrast to MoS₂/P and A-MoS_{2.30}, the MoS_{2.30} owns the worst performance (NH₃ yield rate: 98.30 ± 1.63 μg h⁻¹ mg_{cat}⁻¹ and FE (23.10 ± 0.38%) at -0.5 V vs. RHE, demonstrating the significant enhancement effect of 1T phase on the NRR performance. The NRR performance of all the synthesized catalysts with similar 1T contents but different stoichiometric ratios is shown in Fig. 3a and S13. With the increased stoichiometric ratios, the evolution of the NRR performance shows a “roller-coaster” type and reaches a peak at MoS_{2.30}, and the r-MoS_{2.30} maintaining a high 1T content but lacking bridging S₂²⁻ species exhibits the worst performance (NH₃ yield rate: 64.56 ± 0.62 μg h⁻¹ mg_{cat}⁻¹, FE: 19.85 ± 0.19%), demonstrating that the S₂²⁻ species play a prominent role for NRR. Compared with that under Ar condition, MoS_{2.30} exhibits an improved current density under N₂-saturated K₂SO₄ electrolyte, as determined by linear sweep voltammetry (LSV) curves (Fig. S14a), proving that the sample is active toward NRR at the particular potential window caused by the multiple NRR electronic processes [44,45]. At potentials in the fixed range (-0.4 to -0.8 V), the NRR performance of MoS_{2.30} was assessed by three parallel experiments (Fig. 3b and S15), and the time-current density curves demonstrate exceptional durability with minimal fluctuations at each provided potential (Fig. S14b). It should be noticed that both NH₃ yield rates and FEs are drastically decreased beyond -0.5 V since the competing HER dominate at higher overpotentials [12,46]. Aiming at confirming the validity of the indophenol blue method, different analysis methods, including Nessler’s reagent methods, ion chromatography (IC) methods, and quantified nuclear magnetic resonance (NMR) methods [47–49], have also been conducted (Figs. S16–S19), further verifying the accuracy of the NH₃ detection. Also, an isotopic labeled NMR test was conducted to detect the source of the N component in the produced NH₃ (Fig. 3c). When ¹⁴N₂ gas is provided, the distinctive triplet peaks of ¹⁴NH₄⁺ can be observed, whereas ¹⁵N₂ gas can be employed to detect the doublet peaks associated with ¹⁵NH₄⁺ [50]. Definitive proof that the N in the feeding N₂ serves as the sole origin of the produced NH₃ can be found in the supplementary quantitative NRR

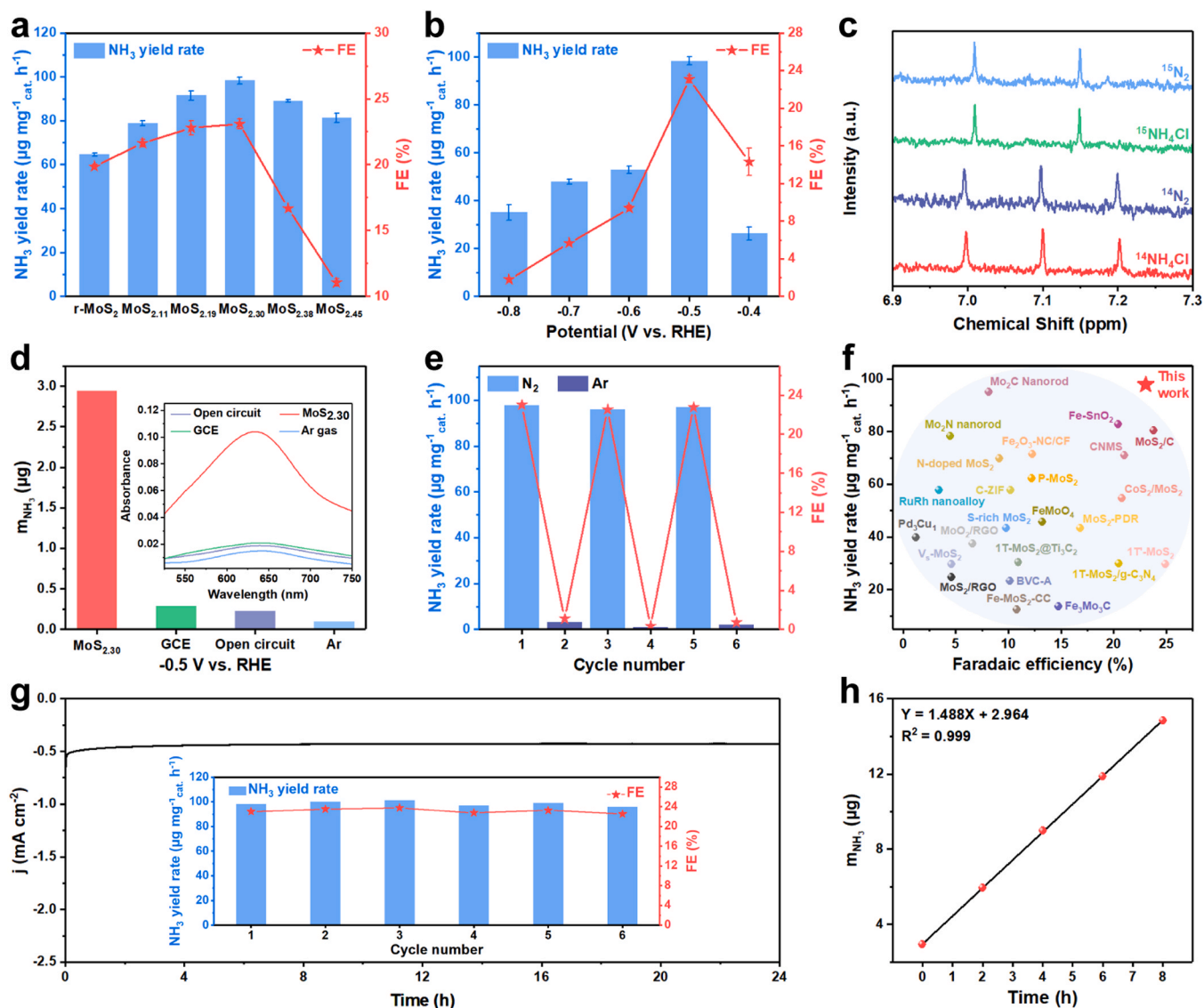


Fig. 3. (a) Comparison of properties (NH₃ yield rates and FEs) at -0.5 V vs. RHE over various catalysts under the same conditions. (b) Properties of MoS_{2.30} at various potentials. (c) ¹H NMR (500 MHz) spectra of solution after electrocatalytic N₂ fixation using MoS_{2.30} as the electrocatalyst in the ¹⁴N₂ or ¹⁵N₂ atmosphere. (d) Amount of NH₃ generated after charging at -0.5 V for 2 h under various conditions. The inset is the UV-vis absorption spectra of the electrolytes stained with an indophenol indicator. (e) NH₃ yield rates and corresponding FEs of MoS_{2.30} with switching 2 h cycles between N₂- and Ar-saturated electrolytes. (f) Comparison of NH₃ yields and FE values of MoS_{2.30} with other reported catalysts. (g) Time-dependent current density curve of MoS_{2.30} at -0.5 V for 24 h. The inset is the stability test of MoS_{2.30} during repeated NRR for six cycles at -0.5 V. (h) Curve of ammonia yield vs reaction time at -0.5 V over MoS_{2.30}.

measurement in Fig. S20. Accordingly, additional controlled experiments were performed (Fig. 3d and e) [51,52]. The generation of equivalent amounts of NH₃ is only detected by the MoS_{2.30} catalyst in an N₂-saturated electrolyte, further highlighting the source of N. Note that no hydrazine is detected in Fig. S21, exemplifying the high selectivity of the MoS_{2.30} for NH₃ production. Therefore, such outstanding performance rendered by MoS_{2.30} is superior to most contemporary NRR electrocatalysts (Fig. 3f and Table S2 in detail).

Fig. 3g depicts a 24-hour electrochemical test that could be employed to assess durability. After six successive cycles, MoS_{2.30} maintains its remarkable electrolytic stability despite just a slight variation in NRR property (the inset in Fig. 3g), which is also demonstrated by strong linear dependence on ammonia yield and electrolysis duration (Fig. 3h). The morphology and structure durability, particularly the 1T phase content and bridging S₂²⁻ species of MoS_{2.30} after the NRR measurement is even supported by a series of analysis in Fig. S22 and Table S3. In light of this, it can be determined that the MoS_{2.30} electrocatalyst has excellent NRR activity, selectivity, and stability.

In-depth, we initially found out the remarkable NRR performance of the MoS_{2.30} catalyst. As displayed in the in-situ Raman spectra (Fig. 4a), the signals around 831 and 1010 cm⁻¹ attributed to the Mo-N bond initially appear at -0.5 V, and their intensity becomes increasingly stronger as time accumulates [41,53–55]. Contrarily, the corresponding signals for 0 min in N₂-saturated solutions and after 50 min electrolysis in Ar-saturated solutions cannot be observed, emphasizing that N₂ chemical absorption and activation occur on the Mo-edge of MoS_{2.30}. Thus, the Mo-edge can be methodically identified as NRR active sites. Nitrogen temperature-programmed desorption (TPD) measurements of MoS_{2.30}, r-MoS_{2.30}, and MoS₂/P (Fig. S23) reveal that the MoS_{2.30} and r-MoS_{2.30} show the signal at a higher temperature compared with MoS₂-P, suggesting a stronger nitrogen adsorption capacity. Meanwhile, the intensity of the TPD signal of MoS_{2.30} is higher than r-MoS_{2.30}, revealing more N₂ absorption owing to more active sites caused by the S-enrichment. In light of the metallic phase, the related electrical impedance spectroscopic (EIS) spectra of all samples (Fig. 4b) show a considerable electron transfer capacity. Aside from the EIS, the electrical

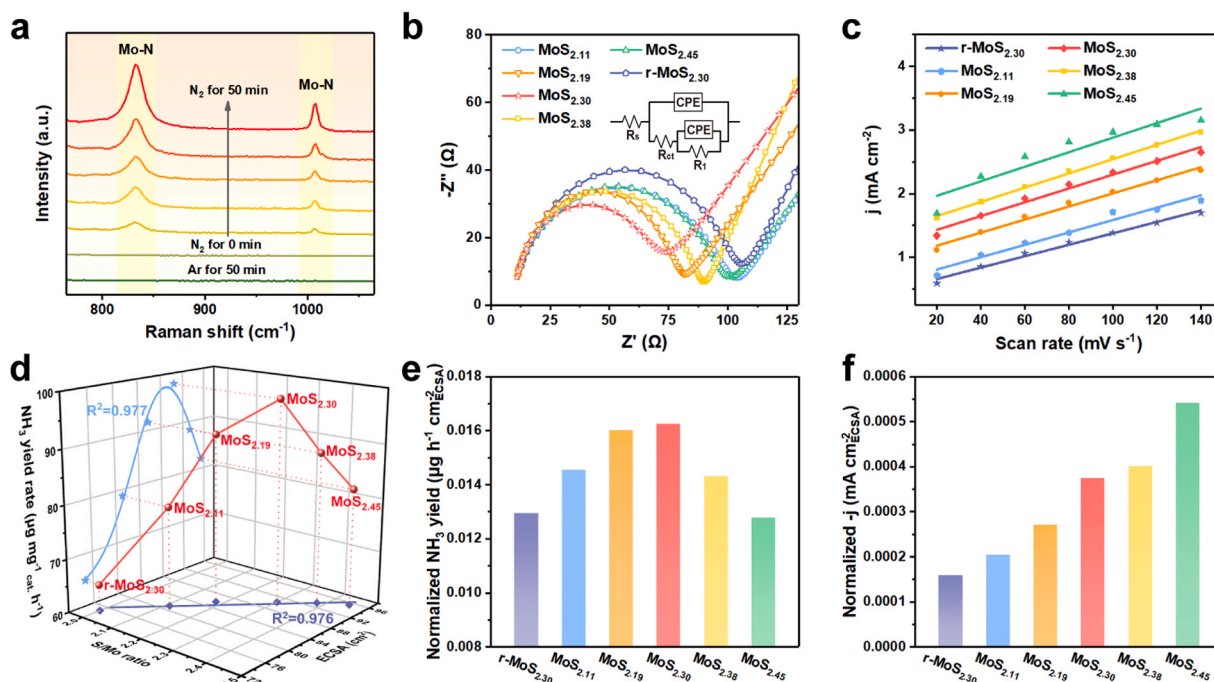


Fig. 4. (a) In situ Raman spectroscopy of MoS_{2.30} at -0.5 V under different conditions. (b) Electrochemical impedance spectroscopy spectra. (c) Measured capacitive currents plotted as a function of the scan rate. (d) Evolution of the NRR performance with the ECSA values and the S/Mo ratios. Evolution of the normalized (e) NH₃ yield rate and (f) current density with various S/Mo ratios at -0.5 V.

conductivity of MoS_{2.30}, r-MoS_{2.30}, and A-MoS_{2.30} has also been conducted (Table S4 and Fig. S24), one can see that the electronic conductivity of the above samples is in the order MoS_{2.30} > r-MoS_{2.30} > A-MoS_{2.30}, strongly indicating the metallic nature of MoS_{2.30} and r-MoS_{2.30} and the semi-conductive property of A-MoS_{2.30}. Those comparisons demonstrate that a higher content of bridging S₂²⁻ species results in a more favorable conductivity [46]. Remarkably, the electrochemical active surface area (ECSA) results (Figs. S25 and 4c; Table S5) increases with stoichiometric ratios and achieves the maximum at MoS_{2.45}, and the nearly linear correlation between ECSA and the amount of bridging S₂²⁻ species (Fig. 4d) reveals that the increased number of active sites may be derived from the amorphous nature (Figs. 1e and 2a) and the introduction of more HER active sites induced by the increased amount of bridging S₂²⁻ species [46,56]. Noteworthy, the deteriorative NRR performance after MoS_{2.30} may be related to the excess bridging S₂²⁻ species as HER active sites. In addition, the normalized NH₃ yield rate and current density measurements (Fig. 4e, f, and S26) were conducted to evaluate the intrinsic activity of NRR and HER, respectively, revealing that the intrinsic activity of NRR and HER strongly rely on the bridging S₂²⁻ species content. The normalized NH₃ yield rate peaks at MoS_{2.30}, while normalized current density monotonically increases with the increased content of bridging S₂²⁻ species, and its growth gradually becomes fast owing to more bridging S₂²⁻, thus leading to the enhanced HER performance (Fig. S26a). Thus, the improved performance before MoS_{2.30} is derived from the NRR activity enhancement caused by the metallic phase- and S-enrichment-induced synergetic effects, including strengthened nitrogen capture (Fig. S23), more active sites (Table S5), and enhanced conductivity (Fig. 4b). Besides, the NRR selectivity on the Mo-edge is remarkably improved due to the optimized competitive adsorption and reduced energy barrier against the HER. In this stage, though the HER activity is also improved resulting from the introduction of bridging S₂²⁻ species (Fig. 4f), the improvement of NRR activity is dominant compared with that of HER so that the yield and FE show a trend of increasing as the ratio of S/Mo increases. However, with the further increase of bridging S₂²⁻ species, the HER activity is further improved as the normalized

current density increases with a gradually rising growth rate. In contrast, the NRR activity slows down with a reduced normalized yield, which indicates that excess bridging S₂²⁻ species may be not prone to NRR by weakening N₂ adsorption or covering the Me-edge sites, thus the yield and FE decrease. Overall, the changes in FE rely on whether the enhancement of NRR activity or HER activity is dominant.

3.3. DFT calculations

To further examine the active sites and fundamentally understand the possibility of the NRR process, the adsorption energy was calculated. Fig. 5a–d shows the structural optimization of various S-rich 1T phase (1T-S₂²⁻-MoS₂) models carried out with freely varying lattice parameters [14]. Model A includes additional S atoms (S^B) bridging MoS₂ slabs, while Model B has extra S atoms bridging to an in-plane S atom (S^I). In model C, one extra S atom was substituted by one Mo atom in each layer (S^{Mo}). Fig. 5d depicts the structure of the configuration Model D, meaning that it emerges when the S^B, S^I, and S^{Mo} atoms coexist. Note that the stoichiometry of four models was set as Mo₂₄S₅₆, Mo₂₄S₅₆, Mo₂₂S₅₀, and Mo₂₃S₅₃, respectively, to approach the stoichiometric ratio of 2.30. The possible NRR process over the models of 1T-S₂²⁻-MoS₂ and 1T-MoS₂ are detailed in Figs. S27–S31 and 5e. Among the four 1T-S₂²⁻-MoS₂ models, though model D has the most positive ΔG_{N₂}, it exhibits the lowest E_b, indicating the most energy-efficient NRR process and strong N₂ adsorption capacity (−1.75 eV). Therefore, model D was selected as the 1T-S₂²⁻-MoS₂ model to investigate the detailed reaction mechanism and make a comparison with 1T-MoS₂ and 2H-MoS₂. Taking both the ΔG_{N₂} and the E_b into account, it is apparent that the 1T-S₂²⁻-MoS₂ (Model D with the optimal NRR process) has the most negative nitrogen adsorption free energy with ΔG_{1T-S₂²⁻-MoS₂ (N-N→N*-N*) = −1.75 eV, suggesting the remarkable contribution of the 1T phase and bridging S₂²⁻ on enhancing the nitrogen adsorption capacity, corresponding to TPD results (Fig. S23). Moreover, the PDS for 1T-S₂²⁻-MoS₂ shows an E_{b-NRR} of 0.32 eV (N*H-NH₂→N*H₂-NH₂ step, the limiting potential (U_L) is −0.32 V), which is lower than those of E_{b-NRR} = 0.36 eV for 1T-MoS₂}

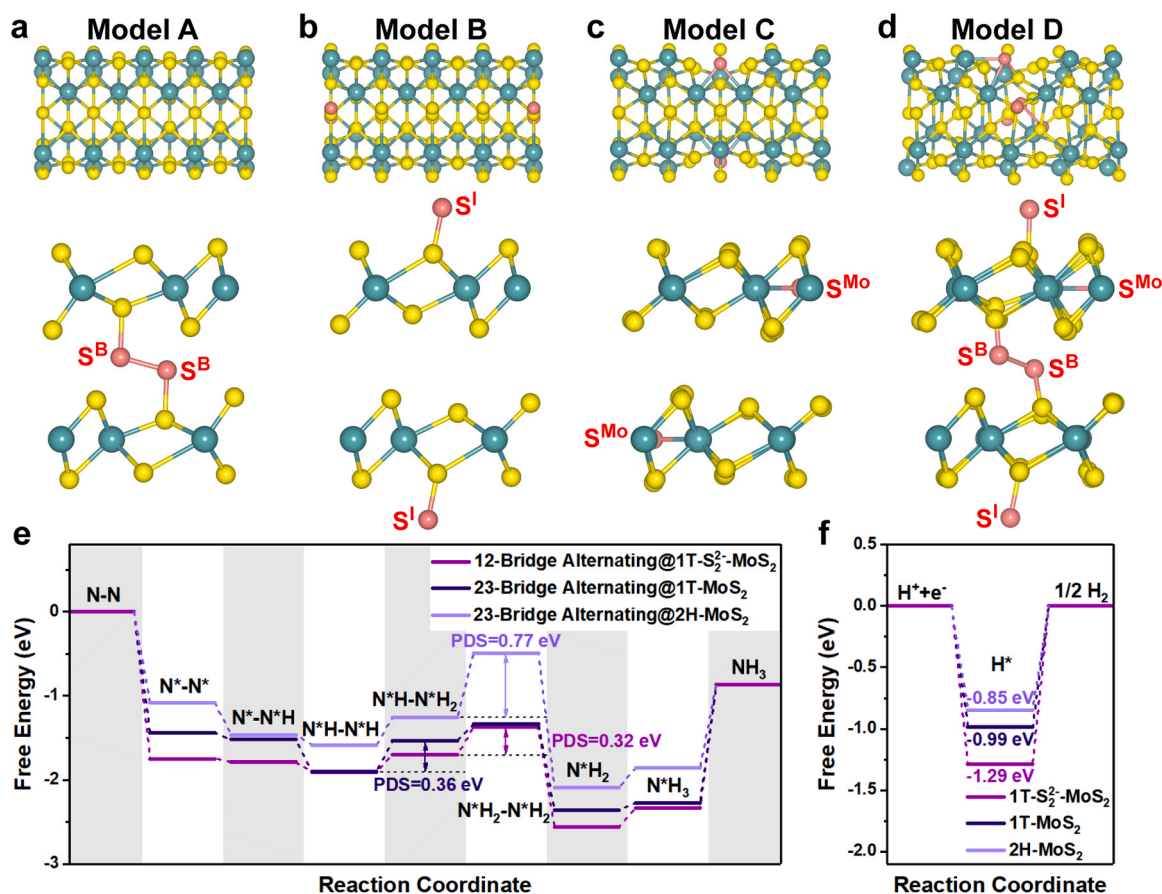


Fig. 5. (a–d) DFT calculation of S-rich 1T phase MoS_x. Blue and yellow balls represent the Mo and S atoms of pristine layers, respectively, and pink balls represent the extra S atoms (S^B, S^I, and S^{Mo}). (e) Gibbs free energy diagrams on the 1T-S₂-MoS₂ (model D) surface along the respective optimum NRR reaction pathway, the 1T-MoS₂ surface, and the 2H-MoS₂ surface. The PDS for each reaction pathway is marked. (f) HER Gibbs free energy diagrams on the 1T-S₂-MoS₂ (model D), 1T-MoS₂, and 2H-MoS₂ surface. The asterisk * in (e) and (f) denotes the atom in the adsorbate, which is bound to the 1T-S₂-MoS₂, the 1T-MoS₂, and the 2H-MoS₂ surface. The common intermediates for all reaction pathways on the 1T-S₂-MoS₂, the 1T-MoS₂, and the 2H-MoS₂ surface are denoted in black font.

(N^{*}H-NH→N^{*}H-NH₂ step, U_L = -0.36 V) and $E_{b-2H-MoS_2}^{NRR} = 0.77$ eV for 2H-MoS₂ (N^{*}H-NH₂→N^{*}H₂-NH₂ step, U_L = -0.77 V). Considering the above evaluations, the 1T-S₂-MoS₂ delivers the optimal activity on account of the strongest Mo-N₂ interaction and the lowest E_b. The reason for the optimized activity is confirmed by the charge density difference (Fig. S32) in which an obvious charge increase occurs on the Mo-edge over 1T-S₂-MoS₂, enabling 1T-S₂-MoS₂ to exhibit strengthened N₂ adsorption capacity [12,57].

By making comparisons of the $\Delta G_{\text{adsorbate}}$ and E_b, the competition of NRR and HER can be quantified, which is a critical component that impacts the NRR selectivity of catalysts [12,58]. Fig. 5f and Table S6 demonstrate although exhibiting a negative $\Delta G_{\text{NNH}}-\Delta G_{\text{H}}$ (more stable of *NNH than *H) and E_{b-NRR}-E_{b-HER} (smaller energy barrier), the positive $\Delta G_{\text{N}_2}-\Delta G_{\text{H}}$ at an applied potential of U_{L-2H-MoS2} (-0.77 V) demonstrates the Mo-edge in 2H phase is in favor of being covered with *H as expected, while the later two models with the 1T phase possess negative values of these three descriptors, suggesting the enhancing role of the 1T phase on the NRR selectivity, as displayed in the NRR performance of A-MoS_{2.30} and r-MoS_{2.30} in Figs. S12 and S13a, which agrees well with our previous reports [12,37]. The further comparison indicates that although possessing the comparable competitive adsorption (nearly equal $\Delta G_{\text{N}_2}-\Delta G_{\text{H}}$ and $\Delta G_{\text{NNH}}-\Delta G_{\text{H}}$), the Mo-edge of 1T-S₂-MoS₂ prefers to NRR than that of 1T-MoS₂ with more negative E_{b-NRR}-E_{b-HER}, which reveals a smaller energy barrier of NRR relative to that of HER, thus causing further enhancement of the NRR selectivity, as shown in the NRR performance of MoS_{2.30} and r-MoS_{2.30} in Fig. 3a. Overall, the S-rich 1T-MoS₂ shows enhanced NRR selectivity due to the

optimized competitive adsorption and reduced energy barrier against the HER derived from the synergistic effect between 1T phase and bridging S₂²⁻ species.

Overall, the synergistic effect between 1T phase and bridging S₂²⁻ species in this work can be defined as below: (1) it can further trigger the surrounding electron redistribution compared with the pure 1T-MoS₂ (r-MoS_{2.30}, Fig. S32), thus synchronously improving the intrinsic NRR activity and selectivity on the Mo-edge of MoS_{2.30} by strengthened N₂ adsorption/reduced energy barrier and optimized competitive adsorption, respectively (Fig. 5e and Table S6). (2) The bridging S₂²⁻ species itself together with the resulting amorphous nature of the 1T phase benefits from exposing more active sites (Table S5), contributing to both NRR and HER. (3) The bridging S₂²⁻ species and the metallic 1T phase significantly accelerate the electronic transfer during NRR (Fig. 4b). (4) Some intercalated bridging S₂²⁻ species into the interlayer of MoS_{2.30} may stabilize the 1T phase to some extent, contributing to its excellent stability for long-term NRR (Fig. S22).

4. Conclusions

In summary, the S-rich 1T-MoS₂ with an ultrahigh 1T phase content of 93.31% and S-enrichment has been successfully prepared and firstly verified as an efficient NRR catalyst. The optimized MoS_{2.30} catalyst exhibits an ultrahigh NH₃ yield rate (98.30±1.63 μg h⁻¹ mg_{cat.}⁻¹) and FE (23.10±0.38%), superior to most contemporary NRR electrocatalysts, which suggests the encouraging role-playing of the synergistic effect between 1T phase and bridging S₂²⁻ species on NRR performances. DFT

calculations reveal such enhanced performance of MoS_{2.30} is attributed to two aspects: (i) The activity could be elevated via the strengthened N₂ adsorption and reduced energy barrier due to the synergistic effect; (ii) The selectivity could be simultaneously enhanced through the optimized competitive adsorption and reduced energy barrier against HER derived from the synergistic effect. This work delivers a superb catalyst and offers a novel perspective toward regulating the active sites for NRR and other catalytic fields.

CRedit authorship contribution statement

Ruoqi Liu: Investigation, Data curation, Visualization, Writing-Original Draft. **Hao Fei:** Formal analysis, Writing-Review & Editing. **Jian Wang:** Writing-Review & Editing. **Ting Guo:** Software, Formal analysis. **Fangyang Liu:** Writing-Review & Editing. **Zhuangzhi Wu:** Conceptualization, Writing-Review & Editing, Supervision. **Dezhi Wang:** Supervision.

Declaration of Competing Interest

The authors declare that they have no known competing financial interests or personal relationships that could have appeared to influence the work reported in this paper.

Data Availability

Data will be made available on request.

Acknowledgements

Financial support from the National Natural Science Foundation of China (Grant No. 52374407) is gratefully acknowledged.

Appendix A. Supporting information

Supplementary data associated with this article can be found in the online version at doi:10.1016/j.apcatb.2023.123469.

References

- N. Gruber, J. Galloway, An earth-system perspective of the global nitrogen cycle, *Nature* 451 (2008) 293–296, <https://doi.org/10.1038/nature06592>.
- D.R. MacFarlane, P.V. Cherepanov, J. Choi, B.H.R. Suryanto, R.Y. Hodgetts, J. M. Bakker, F.M. Ferrero Vallana, A.N. Simonov, A Roadmap Ammon. Econ., *Joule* 4 (2020) 1186–1205, <https://doi.org/10.1016/j.joule.2020.04.004>.
- Y. Liu, L. Wang, L. Chen, H. Wang, A.R. Jadhav, T. Yang, Y. Wang, J. Zhang, A. Kumar, J. Lee, V.Q. Bui, M.G. Kim, H. Lee, Unveiling the protonation kinetics-dependent selectivity in nitrogen electroreduction: achieving 75.05% selectivity, *Angew. Chem., Int. Ed.* 6 (2022), e202209555, <https://doi.org/10.1002/anie.202209555>.
- F.B. Fan, H.Z. Wang, H. Zhang, Y. Song, X.R. Zheng, C.J. Li, Y.Q. Tan, X.P. Han, Y. D. Deng, W.B. Hu, Phase transfer of Mo₂C induced by boron doping to boost nitrogen reduction reaction catalytic activity, *Adv. Funct. Mater.* 32 (2022), 2110783, <https://doi.org/10.1002/adfm.202110783>.
- S. Chung, H. Ju, M. Choi, D. Yoon, J. Lee, Local proton source enhanced nitrogen reduction on a combined cobalt-molybdenum catalyst for electrochemical ammonia synthesis, *Angew. Chem., Int. Ed.* 61 (2022), e202212676, <https://doi.org/10.1002/anie.202212676>.
- G.X. Lin, Q.J. Ju, X.W. Guo, W. Zhao, S. Adimi, J.Y. Ye, Q.Y. Bi, J.C. Wang, M. H. Yang, F.Q. Huang, Intrinsic electron localization of metastable MoS₂ boosts electrocatalytic nitrogen reduction to ammonia, *Adv. Mater.* 33 (2021), 2007509, <https://doi.org/10.1002/adma.202007509>.
- Y.Y. Liu, M.M. Han, Q.Z. Xiong, S.B. Zhang, C.J. Zhao, W.B. Gong, G.Z. Wang, H. M. Zhang, H.J. Zhao, Dramatically enhanced ambient ammonia electrosynthesis performance by in-operando created Li-S interactions on MoS₂ electrocatalyst, *Adv. Energy Mater.* 9 (2019), 1803935, <https://doi.org/10.1002/aenm.201803935>.
- J. Zhang, X.Y. Tian, M.J. Liu, H. Guo, J.D. Zhou, Q.Y. Fang, Z. Liu, Q. Wu, J. Lou, Cobalt-modulated molybdenum-dinitrogen interaction in MoS₂ for catalyzing ammonia synthesis, *J. Am. Chem. Soc.* 141 (2019) 19269–19275, <https://doi.org/10.1021/jacs.9b02501>.
- T.F. Jaramillo, K.P. Jørgensen, J. Bonde, J.H. Nielsen, S. Hørch, I. Chorkendorff, Identification of active edge sites for electrochemical H₂ evolution from MoS₂ nanocatalysts, *Science* 317 (2007) 100–102, <https://doi.org/10.1126/science.1141483>.
- Y. Yu, G.H. Nam, Q. He, X.J. Wu, K. Zhang, Z. Yang, J. Chen, Q. Ma, M. Zhao, Z. Liu, F.R. Ran, X. Wang, H. Li, X. Huang, B. Li, Q. Xiong, Q. Zhang, Z. Liu, L. Gu, Y. Du, W. Huang, H. Zhang, High phase-purity 1T'-MoS₂- and 1T'-MoSe₂-layered crystals, *Nat. Chem.* 10 (2018) 638–643, <https://doi.org/10.1038/s41557-018-0035-6>.
- X.S. Xu, X.J. Tian, B.T. Sun, Z.Q. Liang, H.Z. Cui, J. Tian, M.H. Shao, 1 T-phase molybdenum sulfide nanodots enable efficient electrocatalytic nitrogen fixation under ambient conditions, *Appl. Catal., B* 272 (2020), 118984, <https://doi.org/10.1016/j.apcatb.2020.118984>.
- R.Q. Liu, T. Guo, H. Fei, Z.Z. Wu, D.Z. Wang, F.Y. Liu, Highly efficient electrocatalytic N₂ reduction to ammonia over metallic 1T phase of MoS₂ enabled by active sites separation mechanism, *Adv. Sci.* 9 (2022), 2103583, <https://doi.org/10.1002/adv.202103583>.
- J.J. Guo, M.Y. Wang, L. Xu, X.M. Li, A. Iqbal, G.E. Sterbinsky, H. Yang, M. Xie, J. T. Zai, Z.X. Feng, T. Cheng, X.F. Qian, Bioinspired activation of N₂ on asymmetrical coordinated Fe grafted 1T MoS₂ at room temperature, *Chin. J. Chem.* 39 (2021) 1898–1904, <https://doi.org/10.1002/cjoc.202000675>.
- I.S. Kwon, I.H. Kwak, T.T. Debela, H.G. Abbas, Y.C. Park, J.P. Ahn, J. Park, H. S. Kang, Se-Rich MoS₂ nanosheets and their superior electrocatalytic performance for hydrogen evolution reaction, *ACS Nano* 14 (2020) 6295–6304, <https://doi.org/10.1021/acsnano.0c02593>.
- J.D. Li, A. Listwan, J.X. Liang, F. Shi, K. Li, J.P. Jia, High proportion of 1 T phase MoS₂ prepared by a simple solvothermal method for high-efficiency electrocatalytic hydrogen evolution, *Chem. Eng. J.* 422 (2021), 130100, <https://doi.org/10.1016/j.cej.2021.130100>.
- J. Bai, B.Z. Zhao, J.F. Zhou, J.G. Si, Z.T. Fang, K.Z. Li, H.Y. Ma, J.M. Dai, X.B. Zhu, Y.P. Sun, Glucose-induced synthesis of 1T-MoS₂/C hybrid for high-rate lithium-ion batteries, *Small* 15 (2019), 1805420, <https://doi.org/10.1002/sml.201805420>.
- S.S. Chou, N. Sai, P. Lu, E.N. Coker, S. Liu, K. Artyushkova, T.S. Luk, B. Kaehr, C. J. Brinker, Understanding catalysis in a multiphase two-dimensional transition metal dichalcogenide, *Nat. Commun.* 6 (2015) 8311, <https://doi.org/10.1038/ncomms9311>.
- R. Raja, P. Sudhagar, A. Devadoss, C. Terashima, L.K. Shrestha, K. Nakat, R. Jayavel, K. Ariga, A. Fujishima, Pt-free solar driven photoelectrochemical hydrogen fuel generation using 1T MoS₂ co-catalyst assembled CdS QDs/TiO₂ photoelectrode, *Chem. Commun.* 51 (2015) 522, <https://doi.org/10.1039/C4CC07304E>.
- J.F. Xie, H. Zhang, S. Li, R.X. Wang, X. Sun, M. Zhou, J.F. Zhou, X.W. Lou, Y. Xie, Defect-rich MoS₂ ultrathin nanosheets with additional active edge sites for enhanced electrocatalytic hydrogen evolution, *Adv. Mater.* 25 (2013) 5807–5813, <https://doi.org/10.1002/adma.201302685>.
- J.F. Xie, C.Z. Wu, S.L. Hu, J. Dai, N. Zhang, J. Feng, J.L. Yang, Y. Xie, Ambient rutile VO₂(R) hollow hierarchitectures with rich grain boundaries from new-state nsutite-type VO₂, displaying enhanced hydrogen adsorption behavior, *Phys. Chem. Chem. Phys.* 14 (2012) 4810–4816, <https://doi.org/10.1039/c2cp40409e>.
- M. Acerce, D. Voiry, M. Chhowalla, Metallic 1T phase MoS₂ nanosheets as supercapacitor electrode materials, *Nat. Nanotech* 10 (2015) 313–318, <https://doi.org/10.1038/nnano.2015.40>.
- L. Cai, J.F. He, Q.H. Liu, T. Yao, L. Chen, W.S. Yan, F.C. Hu, Y. Jiang, Y.D. Zhao, T. D. Hu, Z.H. Sun, S.Q. Wei, Vacancy-induced ferromagnetism of MoS₂ nanosheets, *J. Am. Chem. Soc.* 137 (2015) 2622–2627, <https://doi.org/10.1021/ja5120908>.
- J.Y. Wang, J. Tang, T. Guo, S.H. Zhang, W. Xia, H.B. Tan, Y. Bando, X. Wang, Y. Yamauchi, C₃N₄-digested 3D construction of hierarchical metallic phase MoS₂, *Nanostruct., J. Mater. Chem. A* 7 (2019) 18388–18396, <https://doi.org/10.1039/C9TA06115K>.
- S. Wang, D. Zhang, B. Li, C. Zhang, Z. Du, H. Yin, X. Bi, S. Yang, Ultrastable In-Plane 1T'-2H MoS₂ Heterostructures for enhanced hydrogen evolution reaction, *Adv. Energy Mater.* 8 (2018), 1801345, <https://doi.org/10.1002/aenm.201801345>.
- X.T. Li, X.D. Lv, N. Li, J.J. Wu, Y.Z. Zheng, X. Tao, One-step hydrothermal synthesis of high-percentage 1T-phase MoS₂ quantum dots for remarkably enhanced visible-light-driven photocatalytic H₂ evolution, *Appl. Catal., B* 243 (2019) 76–85, <https://doi.org/10.1016/j.apcatb.2018.10.033>.
- P.F. Cheng, K. Sun, Y.H. Hu, Memristive behavior and ideal memristor of 1T phase MoS₂ nanosheets, *Nano Lett.* 16 (2016) 572–576, <https://doi.org/10.1021/acs.nanolett.5b04260>.
- H. Li, Q. Zhang, C.C.R. Yap, B.K. Tay, T.H.T. Edwin, A. Olivier, D. Baillargeat, From bulk to monolayer MoS₂: evolution of Raman scattering, *Adv. Funct. Mater.* 22 (2012) 1385–1390, <https://doi.org/10.1002/adfm.201102111>.
- L. Ji, P.F. Yan, C.H. Zhu, C.Y. Ma, W.Z. Wu, C. Wei, Y.L. Shen, S.Q. Chu, J.O. Wang, Y. Du, J. Chen, X.N. Yang, Q. Xu, One-pot synthesis of porous 1T-phase MoS₂ integrated with single-atom Cu doping for enhancing electrocatalytic hydrogen evolution reaction, *Appl. Catal., B* 251 (2019) 87–93, <https://doi.org/10.1016/j.apcatb.2019.03.053>.
- X.M. Geng, Y.C. Jiao, Y. Han, A. Mukhopadhyay, L. Yang, H.L. Zhu, Freestanding metallic 1T MoS₂ with dual ion diffusion paths as high rate anode for sodium-ion batteries, *Adv. Funct. Mater.* 27 (2017), 1702998, <https://doi.org/10.1002/adfm.201702998>.
- R.Q. Ye, P.D.A. Vicente, Y.Y. Liu, M.J.A. Jimenez, Z.W. Peng, T. Wang, Y.L. Li, B. I. Yakobson, S.H. Wei, M.J. Yacaman, J.M. Tour, High-performance hydrogen evolution from MoS₂(1-x)Px solid solution, *Adv. Mater.* 28 (2016) 1427–1432, <https://doi.org/10.1002/adma.201504866>.
- B. Vedhanarayanan, J. Shi, J.Y. Lin, S.N. Yun, T.W. Lin, Enhanced activity and stability of MoS₂ through enriching 1T-phase by covalent functionalization for energy conversion applications, *Chem. Eng. J.* 403 (2021), 126318, <https://doi.org/10.1016/j.cej.2020.126318>.

- [32] R. Zhang, J.K. Wang, C. Li, T. Liu, T.H. Yao, L. Zhu, X.G. Han, H.K. Wang, Facile synthesis of hybrid MoS₂/graphene nanosheets as high-performance anode for sodium-ion batteries, *Ionics* 26 (2020) 711–717, <https://doi.org/10.1007/s11581-019-03235-7>.
- [33] T.W. Lin, C.J. Liu, J.Y. Lin, Facile synthesis of MoS₃/carbon nanotube nanocomposite with high catalytic activity toward hydrogen evolution reaction, *Appl. Catal., B* 134–135 (2013) 75–82, <https://doi.org/10.1016/j.apcatb.2013.01.004>.
- [34] T. Bourgeteau, D. Tondelier, B. Geffroy, R. Brisse, C.L. Robert, S. Campidelli, R. Bettignies, V. Artero, S. Palacin, B. Jusselme, A H₂-evolving photocathode based on direct sensitization of MoS₃ with an organic photovoltaic cell, *Energy Environ. Sci.* 6 (2013) 2706–2713, <https://doi.org/10.1039/c3ee41321g>.
- [35] Y.Y. Liu, Y. Xie, L.J. Liu, J.L. Jiao, Sulfur vacancy induced high performance for photocatalytic H₂ production over 1T/2H phase MoS₂ nanolayers, *Catal. Sci. Technol.* 7 (2017) 5635–5643, <https://doi.org/10.1039/c7cy01488k>.
- [36] C.H. Lee, S.H. Lee, G.S. Kang, Y.K. Lee, G.G. Park, D.C. Lee, H.I. Joh, Insight into the superior activity of bridging sulfur-rich amorphous molybdenum sulfide for electrochemical hydrogen evolution reaction, *Appl. Catal., B* 258 (2019) 117995, <https://doi.org/10.1016/j.apcatb.2019.117995>.
- [37] R.Q. Liu, H. Fei, J. Wang, T. Guo, F.Y. Liu, J.Y. Wang, Z.Z. Wu, D.Z. Wang, Insights of active sites separation mechanism for highly efficient electrocatalytic N₂ reduction to ammonia over glucose-induced metallic MoS₂, *Appl. Catal., B* 337 (2023), 122997, <https://doi.org/10.1016/j.apcatb.2023.122997>.
- [38] Y.C. Lin, D.O. Dumcenco, Y.S. Huang, K. Suenaga, Atomic mechanism of the semiconducting-to-metallic phase transition in single-layered MoS₂, *Nat. Nanotech* 9 (2014) 391–396, <https://doi.org/10.1038/nnano.2014.64>.
- [39] Z.Q. Liu, K.K. Nie, X.Y. Qu, X.H. Li, B.J. Li, Y.L. Yuan, S.K. Chong, P. Liu, Y.G. Li, Z. Y. Yin, W. Huang, General bottom-up colloidal synthesis of nano-monolayer transition-metal dichalcogenides with high 1T'-phase purity, *J. Am. Chem. Soc.* 144 (2022) 863–8873, <https://doi.org/10.1021/jacs.1c12379>.
- [40] Q. Liu, X.L. Li, Q. He, A. Khalil, D.B. Liu, T. Xiang, X.J. Wu, L. Song, Gram-scale aqueous synthesis of stable few-layered 1T-MoS₂: applications for visible-light-driven photocatalytic hydrogen evolution, *Small* 11 (2015) 5556–5564, <https://doi.org/10.1002/sml.201501822>.
- [41] H. Fei, R.Q. Liu, J. Wang, T. Guo, Z.Z. Wu, D.Z. Wang, F.Y. Liu, Targeted modulation of competitive active sites toward nitrogen fixation via sulfur vacancy engineering over MoS₂, *Adv. Funct. Mater.* (2023), 2302501, <https://doi.org/10.1002/adfm.202302501>.
- [42] M.F. Wang, S.S. Liu, H.Q. Ji, T.Z. Yang, T. Qian, C.L. Yan, Salting-out effect promoting highly efficient ambient ammonia synthesis, *Nat. Commun.* 12 (2021) 3198, <https://doi.org/10.1038/s41467-021-23360-0>.
- [43] B.H.R. Suryanto, H.L. Du, D.B. Wang, J. Chen, A.N. Simonov, D.R. MacFarlane, Challenges and prospects in the catalysis of electroreduction of nitrogen to ammonia, *Nat. Catal.* 2 (2019) 290–296, <https://doi.org/10.1038/s41929-019-0252-4>.
- [44] P. Li, Z. Jin, Z. Fang, G. Yu, A surface-strained and geometry-tailored nanoreactor that promotes ammonia electrosynthesis, *Angew. Chem. Int. Ed.* 59 (2020) 22610–22616, <https://doi.org/10.1002/anie.202011596>.
- [45] Y. Kong, Y. Li, X.H. Sang, B. Yang, Z.J. Li, S.X. Zheng, Q.H. Zhang, S.Y. Yao, X. X. Yang, L.C. Lei, S.D. Zhou, G. Wu, Y. Hou, Atomically dispersed zinc (I) active sites to accelerate nitrogen reduction kinetics for ammonia electrosynthesis, *Adv. Mater.* 34 (2021), 2103548, <https://doi.org/10.1002/adma.202103548>.
- [46] H. Fei, T. Guo, Y. Xin, L.B. Wang, R.Q. Liu, D.Z. Wang, F.Y. Liu, Z.Z. Wu, Sulfur vacancy engineering of MoS₂ via phosphorus incorporation for improved electrocatalytic N₂ reduction to NH₃, *Appl. Catal., B* 300 (2022), 120733, <https://doi.org/10.1016/j.apcatb.2021.120733>.
- [47] H.Y. Su, L.L. Chen, Y.Z. Chen, R. Si, Y.T. Wu, X.N. Wu, Z.G. Geng, W.H. Zhang, J. Zeng, Single atoms of iron on MoS₂ nanosheets for N₂ electroreduction into ammonia, *Angew. Chem. Int. Ed.* 59 (2020) 20411–20416, <https://doi.org/10.1002/anie.202009217>.
- [48] Y. Li, Y.X. Ji, Y.J. Zhao, J.X. Chen, S.X. Zheng, X.H. Sang, B. Yang, Z.J. Li, L.C. Lei, Z.H. Wen, X.L. Feng, Y. Hou, Local spin-state tuning of iron single-atom electrocatalyst by S-coordinated doping for kinetics-boosted ammonia synthesis, *Adv. Mater.* 34 (2022), 2202240, <https://doi.org/10.1002/adma.202202240>.
- [49] M.D. Liu, S. Zhang, M. Chen, L.M. Wu, Boosting electrochemical nitrogen reduction performance through water-in-salt electrolyte, *Appl. Catal., B* 319 (2022), 121925, <https://doi.org/10.1016/j.apcatb.2022.121925>.
- [50] M.L. Yang, X.M. Wang, C.J. Gómez-García, Z.X. Jin, J.J. Xin, X.X. Cao, H.Y. Ma, H. J. Pang, L.C. Tan, G.X. Yang, Y.H. Kan, Efficient electron transfer from an electron-reservoir polyoxometalate to dual-metal-site metal-organic frameworks for highly efficient electroreduction of nitrogen, *Adv. Funct. Mater.* 33 (2023), 2214495, <https://doi.org/10.1002/adfm.202214495>.
- [51] K. Chen, J.X. Wang, J.L. Kang, X.B. Lu, X.L. Zhao, K. Chu, Atomically Fe-doped MoS_{2-x} with Fe-Mo dual sites for efficient electrocatalytic NO reduction to NH₃, *Appl. Catal., B* 324 (2023), 122241, <https://doi.org/10.1016/j.apcatb.2022.122241>.
- [52] K. Chu, Y.P. Liu, Y.B. Li, Y.L. Guo, Y. Tian, H. Zhang, Multi-functional Mo-doping in MnO₂ nanoflowers toward efficient and robust electrocatalytic nitrogen fixation, *Appl. Catal., B* 264 (2020), 118525, <https://doi.org/10.1016/j.apcatb.2019.118525>.
- [53] K. Chu, Y.J. Luo, P. Shen, X.C. Li, Q.Q. Li, Y.L. Guo, Unveiling the synergy of O-vacancy and heterostructure over MoO_{3-x}/MXene for N₂ electroreduction to NH₃, *Adv. Energy Mater.* 12 (2022), 2103022, <https://doi.org/10.1002/aenm.202103022>.
- [54] H.M. Guan, W.C. Yi, T. Li, Y.H. Li, J.F. Li, H. Bai, G.C. Xi, Low temperature synthesis of plasmonic molybdenum nitride nanosheets for surface enhanced Raman scattering, *Nat. Commun.* 11 (2020) 3889, <https://doi.org/10.1038/s41467-020-17628-0>.
- [55] M. Genelot, N.P. Cheval, M. Vitorino, E. Berrier, J.M. Weibel, P. Pale, A. Mortreux, R.M. Gauvin, Well-defined silica-supported molybdenum nitride species: silica grafting triggers alkyne metathesis activity, *Chem. Sci.* 4 (2013) 2680, <https://doi.org/10.1039/C3SC50325A>.
- [56] L.R.L. Ting, Y.L. Deng, L. Ma, Y.J. Zhang, A.A. Peterson, B.S. Yeo, Catalytic activities of sulfur atoms in amorphous molybdenum sulfide for the electrochemical hydrogen evolution reaction, *ACS Catal.* 6 (2016) 861–867, <https://doi.org/10.1021/acscatal.5b02369>.
- [57] G.L. Fan, W.C. Xu, J.H. Li, J.L. Chen, M. Yu, Y.X. Ni, S.L. Zhu, X.C. Su, F.Y. Cheng, Nanoporous NiSb to enhance nitrogen electroreduction via tailoring competitive adsorption sites, *Adv. Mater.* 33 (2021), 2101126, <https://doi.org/10.1002/adma.202101126>.
- [58] Y.Y. Ma, T. Yang, H.Y. Zou, W.J. Zang, Z.K. Kou, L. Mao, Y.P. Feng, L. Shen, S. J. Pennycook, L.L. Duan, X. Li, J. Wang, Synergizing Mo single atoms and Mo₂C nanoparticles on CNTs synchronizes selectivity and activity of electrocatalytic N₂ reduction to ammonia, *Adv. Mater.* 32 (2020), 2002177, <https://doi.org/10.1002/adma.202002177>.